Computational Mechanics (2018) 62:1009–1021
https://doi.org/10.1007/s00466-018-1547-z

ORIGINAL PAPER

Isogeometric frictionless contact analysis with the third medium method

R. Kruse[1] · N. Nguyen-Thanh[1] · P. Wriggers[2] · L. De Lorenzis[1]

Received: 24 October 2017 / Accepted: 2 January 2018 / Published online: 23 January 2018

Abstract
This paper presents an isogeometric formulation for frictionless contact between deformable bodies, based on the recently proposed concept of the third medium. This concept relies on continuum formulations not only for the contacting bodies but also for a fictitious intermediate medium in which the bodies can move and interact. Key to the formulation is a suitable definition of the constitutive behavior of the third medium. In this work, based on a number of numerical tests, the role of the material parameters of the third medium is systematically assessed. We also assess the rate of spatial convergence for higher-order discretizations, stemming from the regularization of the non-smooth contact problem inherent to the third medium approach. Finally, problems with self contact are considered and turn out to be an attractive application of the method.

Keywords Contact mechanics · Isogeometric analysis · NURBS · Third medium method

1 Introduction

A wide range of methods is available to deal with contact mechanics within a finite element discretization setting, for an overview see e.g. [1,2]. The methods may be categorized by the way they formulate and discretize the contact contribution in the weak form (here we can mention the classical node-to-surface approach and the more recently emerged mortar method), as well as by the mathematical strategy to enforce the unilateral contact constraints (the most common choices being the penalty, the Lagrange multiplier, and the augmented Lagrange multiplier methods). Despite the vast amount of research devoted to the topic and the considerable progress achieved, computational modeling of contact still represents a challenge for the computational analyst.

Recently, Wriggers et al. [3] proposed a new method in which the space between the bodies potentially in contact is filled with a third medium, described as a fictitious material featuring an isotropic/anisotropic behavior with changing directions and characteristics. By proper choice of the constitutive behavior of the third medium, penetration of the bodies is prevented whereas the behavior prior to the onset of contact remains unaffected. The original paper demonstrated the feasibility of the approach and presented a few examples, mainly dealing with no or a limited amount of tangential sliding, within a large deformation finite element setting with linear (Lagrange) basis functions. In this first study, a systematic assessment of the role played by the constants contained in the material model was not conducted and the performance of the method in large sliding was not discussed. A similar approach using a fictitious contact material in combination with higher-order FEM was recently studied by Bog et al. [4]. Though the material model was isotropic in nature, the desired response in compression could be achieved by proper choice of the single model parameter, and a very small remaining gap between the bodies in contact was observed. No investigation was performed on sliding contact.

Isogeometric analysis (IGA) was proposed by Hughes et al. [5] with the original purpose to fill the gap between computer-aided design (CAD) and finite element analysis. In place of the standard Lagrange polynomial basis functions used in the finite element method (FEM), IGA typically adopts the same functions used in CAD for the representation of the geometry, most notably non-uniform rational B-Splines (NURBS). This results, on one side, in the exact reproduction of the CAD geometry within the analysis environment, and at the same time in the possibility of arbitrary

✉ R. Kruse
r.kruse@tu-braunschweig.de

[1] Institut für Angewandte Mechanik, Technische Universität Braunschweig, Pockelsstr. 3, 38106 Braunschweig, Germany

[2] Institut für Kontinuumsmechanik, Leibniz Universität Hannover, Appelstr. 11, 30167 Hannover, Germany

order approximations, with maximum inter-element continuity C^{p-1} for an order-p parameterization, with unchanged geometry. Recent attempts to solve contact problems within the IGA framework (see [6] for a review) demonstrated significant advantages of IGA over conventional FEM, especially for contact problems involving large deformations and large sliding.

The combination of the third medium approach with IGA appears promising for a few reasons. First, IGA is capable of importing the geometry parameterization directly from CAD. Thus the geometry of the two contacting bodies and of the third medium can be defined directly in the CAD environment. Second, IGA was shown to deliver an increased degree of robustness over FEM under severe mesh distortions [7]. This is expected to be useful for contact problems with large deformations and large sliding, where extreme distortions typically take place in the third medium. Finally, IGA offers the possibility to flexibly increase the order of the discretization without any geometry and parameterization change. As the third medium method transforms the non-smooth contact problem into a regularized smooth continuum mechanics problem, it is expected that higher orders of spatial convergence can be achieved.

In light of the above, the present work pursues the following goals:

- investigate the effect of the parameters contained in the material model of the third medium in frictionless contact without or with a significant amount of sliding, with the objective to find an optimal parameter combination for frictionless contact;
- explore the use of the third medium approach within the IGA framework and the related advantages, as well as verify the possibility to achieve higher-order spatial convergence through the higher-order discretization of the continuum;
- investigate self contact as an attractive application of the third medium approach.

The paper is structured as follows: in Sect. 2 the basics of NURBS-based IGA are briefly presented. Sect. 3 introduces the constitutive models for the contacting bodies and the third medium. In Sect. 4, the effect of the constants in the material model for the third medium in frictionless normal and sliding contact is analyzed. Examples including self contact are also presented. Following a comparison between IGA and conventional FEM, the paper ends with some concluding remarks in Sect. 5.

2 Basics of IGA

A B-spline basis of degree p is generated based on a sequence of real numbers called a knot vector

$$\Xi = \left\{\xi_1, \ldots, \xi_{m+p+1}\right\} \tag{1}$$

where $\xi_1 \leq \xi_2 \leq \ldots \leq \xi_{m+p+1}$, each $\xi_i \in \mathbb{R}$ is a knot, and m is the associated number of control points, also equal to the number of basis functions. A univariate B-spline basis function $N_{i,p}(\xi)$ is obtained from the Cox–de Boor recursion formula. Starting from $p = 0$ where

$$N_{i,0}(\xi) = \begin{cases} 1 & \xi_i \leq \xi < \xi_{i+1} \\ 0 & \text{otherwise} \end{cases} \tag{2}$$

the basis functions for $p > 0$ are obtained from

$$N_{i,p}(\xi) = \frac{\xi - \xi_i}{\xi_{i+p} - \xi_i} N_{i,p-1}(\xi) + \frac{\xi_{i+p+1} - \xi}{\xi_{i+p+1} - \xi_{i+1}} N_{i+1,p-1}(\xi) \tag{3}$$

introducing the convention $0/0 = 0$. If a knot has multiplicity k, the smoothness of the B-spline basis is C^{p-k} at that location. In open knot vectors, the first $p + 1$ knots and the last $p + 1$ terms are equal, so that the basis is interpolatory at the ends.

Once the basis functions are available, a B-spline curve can be constructed as their linear combination

$$\mathbf{C}(\xi) = \sum_{i=1}^{m} \mathbf{P}_i N_{i,p} \tag{4}$$

where $\mathbf{P}_i \in \mathbb{R}^{d_s}$ are the so-called control points, and d_s is the dimension of the physical space.

Multivariate B-splines are generated through the tensor product of univariate B-splines. If d_p denotes the dimension of the parametric space, d_p univariate knot vectors are needed:

$$\Xi^d = \left\{\xi_1^d, \ldots, \xi_{m_d+p_d+1}^d\right\} \tag{5}$$

where $d = 1, \ldots, d_p$, p_d is the polynomial degree in the parametric direction d, and m_d is the associated number of basis functions. Denoting the univariate basis functions in each parametric direction d as N_{i_d,p_d}^d, the multivariate basis functions $B_{\mathbf{i},\mathbf{p}}(\boldsymbol{\xi})$ are obtained from

$$B_{\mathbf{i},\mathbf{p}}(\boldsymbol{\xi}) = \prod_{d=1}^{d_p} N_{i_d,p_d}^d\left(\xi^d\right) \tag{6}$$

where the multi-index $\mathbf{i} = \left\{i_1, \ldots, i_{d_p}\right\}$ denotes the position in the tensor product structure, $\mathbf{p} = \{p_1, \ldots, p_d\}$ indicates the polynomial degree, and $\boldsymbol{\xi} = \left\{\xi^1, \ldots, \xi^{d_p}\right\}$ is the vector of the parametric coordinates in each parametric direction d. B-spline surfaces and solids are obtained for $d_p = 2$ and

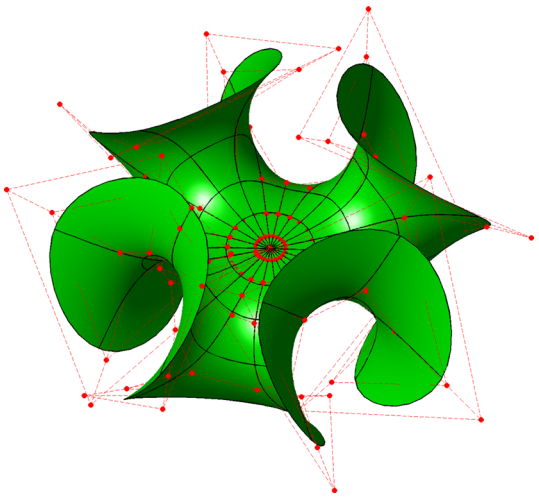

Fig. 1 Physical mesh (green) and control points (red) for a NURBS surface of order $p = 3$. (Color figure online)

$d_p = 3$, respectively, from a linear combination of multivariate B-spline basis functions and control points as follows

$$\mathbf{S}(\boldsymbol{\xi}) = \sum_{\mathbf{i}} \mathbf{P}_{\mathbf{i}} B_{\mathbf{i},\mathbf{p}}(\boldsymbol{\xi}) \tag{7}$$

where the summation is extended to all combinations of the multi-index $\mathbf{i}$.

NURBS basis functions are obtained from a projective transformation of their B-spline counterparts in $\mathbb{R}^{d_s+1}$. Univariate NURBS basis functions $R_{i,p}(\xi)$ are given by

$$R_{i,p}(\xi) = \frac{w_i N_{i,p}(\xi)}{\sum_{j=1}^{m} w_j N_{j,p}(\xi)} \tag{8}$$

where $N_{i,p}$ are B-spline basis functions and w_i are the corresponding weights. Finally, multivariate NURBS basis functions are obtained as

$$R_{\mathbf{i},\mathbf{p}}(\boldsymbol{\xi}) = \frac{w_{\mathbf{i}} B_{\mathbf{i},\mathbf{p}}(\boldsymbol{\xi})}{\sum_{\mathbf{j}} w_{\mathbf{j}} B_{\mathbf{j},\mathbf{p}}(\boldsymbol{\xi})} \tag{9}$$

and NURBS surfaces and solids result from

$$\mathbf{S}(\boldsymbol{\xi}) = \sum_{\mathbf{i}} \mathbf{P}_{\mathbf{i}} R_{\mathbf{i},\mathbf{p}}(\boldsymbol{\xi}) \tag{10}$$

An example of the geometric representation of a free-form shape based on cubic NURBS is illustrated in Fig. 1. The figure also includes the control points, which are generally not located on the physical surface.

In IGA, typically NURBS functions are used as basis functions for the discretization of the geometry and (within the isoparametric framework) of the unknown field. The maps of the knot spans in the physical domain represent the (so-called Bézier) elements. As outlined above, a NURBS interpolation has tailorable continuity (maximum C^{p-1} which may be decreased through knot multiplicity) at the element boundary, as opposed to conventional Lagrangian shape functions which only feature C^0 continuity at the element boundaries regardless of the order. NURBS basis functions are not local to individual elements, but their support extends over $p + 1$ elements in each parametric direction. Extensive details on isogeometric basis functions as well as on IGA for the solution of different types of boundary and initial value problems can be found in [8].

3 Continuum mechanics models for the contacting bodies and the third medium

As in [3], we assume the contacting bodies to obey either linear elasticity or hyperelasticity, and the third medium to be hyperelastic. The kinematics is standard and is not repeated herein. The weak form of the balance equations is given by

$$\int_{\mathcal{B}^\alpha} \mathbf{S}^\alpha \cdot \frac{1}{2}\delta\mathbf{C}^\alpha dV - \int_{\mathcal{B}^\alpha} \mathbf{b}^\alpha \cdot \delta\mathbf{u}^\alpha dV - \int_{\Gamma_t^\alpha} \mathbf{t}^\alpha \cdot \delta\mathbf{u}^\alpha dA = 0 \tag{11}$$

$$\int_{\mathcal{B}^\mathcal{M}} \mathbf{S}^M \cdot \frac{1}{2}\delta\mathbf{C}^M dV = 0 \tag{12}$$

for the two bodies and the third medium, respectively. Here $\mathbf{S}$ is the second Piola–Kirchhoff stress tensor, $\mathbf{C}$ is the right Cauchy–Green deformation tensor, $\mathbf{b}$ is the body force vector, $\mathbf{t}$ is the traction vector applied to the Neumann portion of the boundary Γ_t, and $\mathbf{u}$ is the displacement vector. Quantities related to the bodies in contact are denoted by the superscript $\alpha = 1, 2$, whereas those of the third medium are indicated by the superscript M.

In the following we focus on the constitutive relationships, and provide the expressions of the stress and elasticity tensors.

3.1 Constitutive laws of the contacting bodies

For the contacting bodies, the constitutive equations have to represent the physical behavior. Herein, we consider for both bodies either a linearly elastic or a neo-Hookean material behavior, the latter associated with the strain energy densities

$$\Psi^\alpha = \frac{\mu^\alpha}{2}\left(I_1^\alpha - 3\right) - \mu^\alpha \ln J^\alpha + \frac{\Lambda^\alpha}{2}(\ln J^\alpha)^2 \tag{13}$$

where μ^α and Λ^α are the Lamé constants of body $\mathcal{B}^\alpha$, I_1^α is the first invariant of the right Cauchy–Green deformation

tensor $\mathbf{C}^\alpha$ and $J^\alpha = \det\mathbf{F}^\alpha$ is the Jacobian, with $\mathbf{F}^\alpha$ the deformation gradient.

3.2 Constitutive law of the third medium

The constitutive law of the third medium is fictitious and is dictated by the need to effectively reproduce the contact behavior. Wriggers et al. [3] proposed for the strain energy density of the third medium the combination of an isotropic and an anisotropic component, as follows

$$\Psi^M = \Psi^M_{\text{iso}} + \Psi^M_{\text{aniso}} \tag{14}$$

The isotropic part is given by

$$\Psi^M_{\text{iso}} = a_1 I_1^M + a_2 I_2^M + a_3 I_3^M - d \ln\left(\sqrt{I_3^M}\right) \tag{15}$$

where I_1^M, I_2^M, I_3^M are the invariants of $\mathbf{C}^M$, i.e. the right Cauchy–Green deformation tensor of the third medium $\mathcal{B}^M$, and $a_1, a_2, a_3 \geq 0$ are material parameters with $d = 2a_1 + 4a_2 + 2a_3$. These have to be selected in such a way that the stiffness of the third medium is much smaller than the stiffness of the bodies $\mathcal{B}^\alpha$, in order to approximate rigid body motion before the bodies come into contact. Therefore, the material parameters shall obey

$$a_{1,2,3} \ll \mu^\alpha \quad \text{and} \quad a_{1,2,3} \ll \Lambda^\alpha$$

For the considerations to follow in later sections, it is convenient to introduce dimensionless quantities $\tilde{a}_i$, defined by

$$a_{1,2} = \tilde{a}_{1,2}\mu_{\min}, \quad a_3 = \tilde{a}_3 \Lambda_{\min}$$

with $\mu_{\min}$, $\Lambda_{\min}$ as any appropriate parameters describing the stiffness of the contacting bodies with respect to deviatoric and volumetric deformation, here chosen as the minima of the Lamé constants μ^α and Λ^α.

The anisotropic part of the strain energy density of the third medium is given by

$$\Psi^M_{\text{aniso}} = c^M \left[\frac{1}{a_4+1}\right](1-J_4)^{a_4+1} \quad \text{with}$$
$$J_4 = \text{tr}\left(\mathbf{C}^M \mathbf{M}_n\right) \tag{16}$$

Here a_4 is a further (already dimensionless) material constant, and c^M is a stiffness parameter depending on the gap g_n between bodies $\mathcal{B}^\alpha$ (see Fig. 2). The structural tensor $\mathbf{M}_n = \mathbf{N} \otimes \mathbf{N}$ accounts for the fact that, in case of frictionless contact, the interaction between the bodies $\mathcal{B}^\alpha$ can only encompass (compressive) stresses in the direction normal to the contact surface. $\mathbf{N}$ is the contact normal which, such as g_n, would have to be determined locally from geometric considerations. A simple choice for c^M, proposed in [3], is the function

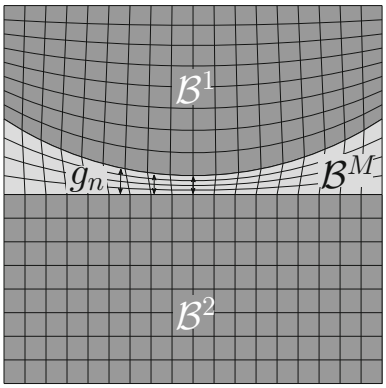

Fig. 2 Contacting bodies $\mathcal{B}^1$ and $\mathcal{B}^2$, separated by a third medium $\mathcal{B}^M$

$$c^M(g_n) = \frac{a_5}{g_n^2} \tag{17}$$

to be used for $g_n \leq d_c$ where d_c is a threshold gap, denoting that the bodies $\mathcal{B}^\alpha$ are close enough to include anisotropic behavior. For $g_n > d_c$ it is $c^M = 0$. As for the previous parameters a_1 to a_3, a dimensionless version of a_5, $\tilde{a}_5$, is introduced via

$$a_5 = \tilde{a}_5 \mu_{\min} \tag{18}$$

The above formulation requires the explicit local geometric determination of the gap size g_n and of the contact normal $\mathbf{N}$. To circumvent this need, in [3] it was proposed to use the minimum principal stretch in the third medium, $\lambda_{\min}$, and its direction, $\mathbf{e}$, obtained from the eigendecomposition of $\mathbf{C}^M$, as measures for g_n and $\mathbf{N}$, respectively. The justification for this idea comes from the observation that, during the approach of the two bodies, the third medium will be highly compressed. Thus, the deformation state of the third medium will be a good indicator for the approach. In the limit of contact, $\lambda_{\min}$ will approach 0 and $\mathbf{e}$ will conform to the surface normal $\mathbf{N}$. Note that this limit will only be approached asymptotically and a residual gap between the bodies will remain (Sect. 4).

The switch criterion $g_n \leq d_c$, substituted through the previous approximation by $\lambda_{\min} \leq \lambda_c$ (with λ_c as a dimensionless threshold), is a source of non-smoothness in the system response, which is undesired. Therefore, in this work we propose a regularized version of the indicator function reading

$$H(\lambda_{\min}) = \frac{1}{2}\left[\cos\left(\frac{\pi}{2\Delta}(\lambda_{\min} - \lambda_c + \Delta)\right) + 1\right] \tag{19}$$

used in the interval $[\lambda_c \pm \Delta]$, with Δ set to 0.1 (equal, as will be shown later, to the lowest investigated value for λ_c),

to avoid the discontinuity in stress and stiffness once the threshold λ_c for the minimum principal strain is reached. This function was applied as a multiplier to the stress tensor associated to the anisotropic strain energy density, $\mathbf{S}_{\text{aniso}}$, see Sect. 3.3 where stress and elasticity tensors stemming from the above formulation are reported.

3.3 Stress and elasticity tensors for the third medium

In the following, stress and elasticity tensors for the third medium are presented. For completeness, all quantities are given both in reference and in current configurations.

3.3.1 Isotropic part

The second Piola–Kirchhoff and the Cauchy stress tensors associated with the isotropic component of the strain energy density, Ψ^M_{iso}, are, respectively, given by

$$\begin{aligned}\mathbf{S}_{\text{iso}} = \quad & 2\left\{\left(a_1 + a_2 I_1^M\right)\mathbf{I} - a_2\mathbf{C}^M \right. \\ & \left. + \left[a_3\left(J^M\right)^2 - \frac{d}{2}\right]\left(\mathbf{C}^M\right)^{-1}\right\}\end{aligned} \tag{20}$$

$$\begin{aligned}\boldsymbol{\sigma}_{\text{iso}} = \quad & \frac{2}{J^M}\left[\left(a_1 + a_2 I_1^M\right)\mathbf{b}^M - a_2\left(\mathbf{b}^M\right)^2 \right. \\ & \left. + \left[a_3\left(J^M\right)^2 - \frac{d}{2}\right]\mathbf{I}\right]\end{aligned} \tag{21}$$

where $\mathbf{I}$ is the second-order identity tensor and $\mathbf{b}$ is the left Cauchy–Green deformation tensor. The Lagrangian and Eulerian elasticity tensors are obtained respectively as

$$\begin{aligned}\mathbb{C}_{\text{iso}} = 4\{ & a_2\left(\mathbf{I}\otimes\mathbf{I} - \mathbb{I}^s\right) \\ & + a_3\left(J^M\right)^2\left[\left(\mathbf{C}^M\right)^{-1}\otimes\left(\mathbf{C}^M\right)^{-1} - \left(\mathbf{C}^M\right)^{-1}\odot\left(\mathbf{C}^M\right)^{-1}\right] \\ & + \frac{d}{2}\left(\mathbf{C}^M\right)^{-1}\odot\left(\mathbf{C}^M\right)^{-1}\Big\}\end{aligned} \tag{22}$$

$$\begin{aligned}c_{\text{iso}} = \frac{4}{J^M}\Big[& a_2\left(\mathbf{b}^M\otimes\mathbf{b}^M - \mathbf{b}^M\odot\mathbf{b}^M\right) \\ & + a_3\left(J^M\right)^2\left(\mathbf{I}\otimes\mathbf{I} - \mathbb{I}^s\right) + \frac{d}{2}\mathbb{I}^s\Big]\end{aligned} \tag{23}$$

where $\mathbb{I}^s$ is the fourth-order symmetric identity tensor. Furthermore the definition

$$(\mathbf{A}\odot\mathbf{A})_{ijkl} = \frac{1}{2}\left(A_{ik}A_{jl} + A_{il}A_{jk}\right) \tag{24}$$

is introduced.

3.3.2 Anisotropic part

The second Piola–Kirchhoff and the Cauchy stress tensors associated with the anisotropic component of the strain energy density, Ψ^M_{aniso}, are, respectively, given by

$$\mathbf{S}_{\text{aniso}} = H(\lambda_{\min})S_a\mathbf{N}\otimes\mathbf{N} \tag{25}$$

$$\boldsymbol{\sigma}_{\text{aniso}} = \frac{1}{J^M}\lambda^2_{\min}H(\lambda_{\min})S_a\mathbf{n}\otimes\mathbf{n} \tag{26}$$

with

$$S_a = -2\frac{a_5}{\lambda^2_{\min}}\left[(1-\lambda^2_{\min})^{a_4} + \frac{1}{\lambda^2_{\min}}\frac{1}{a_4+1}(1-\lambda^2_{\min})^{a_4+1}\right] \tag{27}$$

and $H(\lambda_{\min})$ given by Eq. (19). The Lagrangian and Eulerian elasticity tensors are

$$\mathbb{C}_{\text{aniso}} = \left[H(\lambda_{\min})\bar{\mathbb{C}}_{\text{aniso}} + S_a H'(\lambda_{\min})\right]\mathbf{N}\otimes\mathbf{N}\otimes\mathbf{N}\otimes\mathbf{N} \tag{28}$$

$$c_{\text{aniso}} = \frac{\lambda_{\min}}{J}\left[H(\lambda_{\min})\bar{\mathbb{C}}_{\text{aniso}} + S_a H'(\lambda_{\min})\right]\mathbf{n}\otimes\mathbf{n}\otimes\mathbf{n}\otimes\mathbf{n} \tag{29}$$

where

$$\begin{aligned}\bar{\mathbb{C}}_{\text{aniso}} = & -\frac{2}{\lambda_{\min}}S_a + 4\frac{a_5}{\lambda^3_{\min}} \\ & \left[a_4\lambda^2_{\min}(1-\lambda^2_{\min})^{a_4-1} + \frac{1}{\lambda^2_{\min}}\frac{1}{a_4+1}(1-\lambda^2_{\min})^{a_4+1}\right. \\ & \left. + (1-\lambda^2_{\min})^{a_4}\right]\end{aligned} \tag{30}$$

and

$$H'(\lambda_{\min}) = -\frac{1}{4}\frac{\pi}{\Delta}\sin\left(\frac{\pi}{2\Delta}(\lambda_{\min} - \lambda_c + \Delta)\right) \tag{31}$$

4 Numerical tests and optimal choice of parameters

In this section we present some numerical tests, part of which are used to systematically analyze the role played by the different constants in the material model of the third medium. This analysis is performed for frictionless contact without and with a significant amount of sliding, and for self contact with confined compression of the third medium. Once an optimal parameter combination is identified, the order of spatial convergence for higher-order discretizations is measured. Finally the question of whether IGA offers advantages with respect to conventional higher-order FEM is addressed.

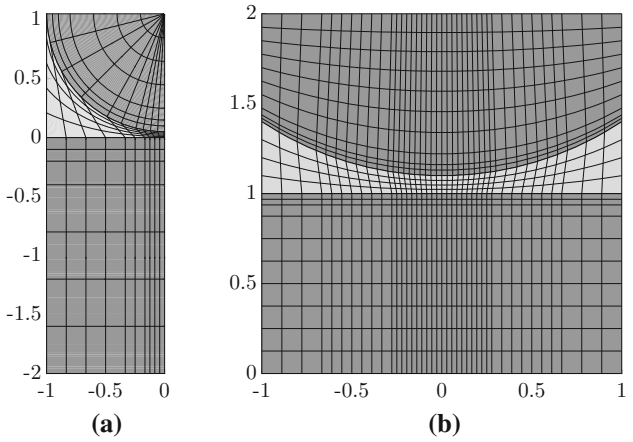

Fig. 3 Hertz contact problems. Symmetry boundary conditions on right edge (**a**) and top edge (**a**, **b**), uniformly distributed loading at the lower edge. Initial (unrefined) mesh shown. Third medium in light gray

Table 1 Hertz example: material parameters of the contacting bodies and applied loads

	E_1	ν_1	E_2	ν_2	P
α_a	7000	0.3	70000	0.45	300 or 100
α_b	700	0.3	7000	0.45	30 or 10

In all examples we adopt full Gauss quadrature. For IGA discretizations this conventionally implies the use of $p+1$ Gauss points per parametric direction per element.

4.1 Normal contact: Hertz problem

The Hertz contact problems considered in this study are shown in Fig. 3. The contacting bodies are linearly elastic with Young's modulus and Poisson's ratios E_1, ν_1 (upper cylinder) and E_2, ν_2 (lower block). Two sets of material parameters for these bodies are considered, see Table 1. Additionally, two load cases for each material parameter combination are chosen, differing in the value of the total applied load. The latter is always applied as a uniform pressure distribution on the lower edge of the specimen. This and all subsequent two-dimensional examples are in plane strain conditions.

The objective of this example is to systematically assess the role of the material parameters of the third medium on the quality of results in a frictionless contact simulation with no or very limited sliding. All simulations were performed with 60 load increments, with the mesh uniformly refined by a factor of 4 compared to Fig. 3, and with NURBS shape functions of order $p=2$ in both parametric directions. All dimensionless parameters of the third medium constitutive law were given three different values, Table 2 provides on overview. Since a_1 and a_2 describe similar mechanical properties of the material, they were set equal to reduce the number of combinations; one of the investigated values for a_4 ($a_4=23$) was chosen as it had been adopted in [3]. All combinations of the given values were used (full block design) and were in turn associated with all material parameter combinations of the contacting bodies and loading conditions in Table 1, as well as with both geometries in Fig. 3.

Table 2 Hertz example: investigated dimensionless material parameters of the third medium

	$\tilde{a}_1, \tilde{a}_2$	$\tilde{a}_3$	a_4	$\tilde{a}_5$	λ_c
M_a	10^{-3}	10^{-3}	1	10^{-3}	0.1
M_b	3×10^{-4}	3×10^{-4}	5	10^{-5}	0.3
M_c	10^{-4}	10^{-4}	23	2×10^{-7}	0.5

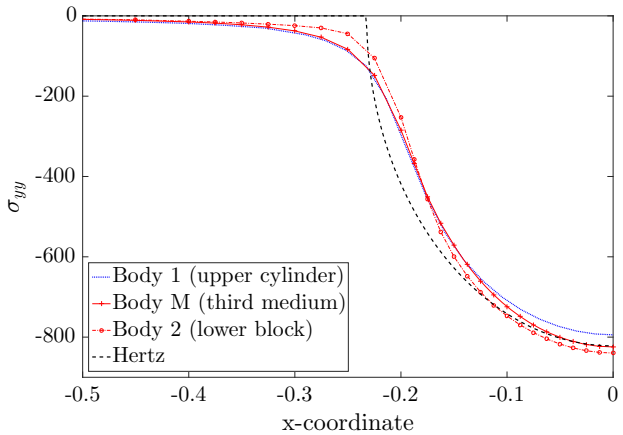

Fig. 4 Hertz example: representative distribution of the Cauchy vertical stress component σ_{yy} (as measure of the contact pressure) from the third medium method, in comparison with the analytical Hertz contact pressure. Geometry (a) from Fig. 3, with load $P=300$ and material properties $(E_1,\nu_1)=(7000,0.3)$, $(E_2,\nu_2)=(70000,0.45)$, $(\tilde{a}_1,\tilde{a}_2,\tilde{a}_3,a_4,\tilde{a}_5,\lambda_c)=(3\cdot10^{-4},3\cdot10^{-4},10^{-4},1,2\cdot10^{-7},0.1)$

The quality of results is measured through the following quantities:

- Gap size: the remaining minimum gap between the bodies (at the center of the specimen).
- Pressure error: the norm of the difference in contact pressure (identified with the vertical Cauchy stress σ_{yy}) relative to the analytical Hertz pressure p_{ref} (eq. 5.52 from [9]), defined as follows

$$p_{\text{err}} = \frac{\sqrt{\sum_i \left(\sigma_{yy}^{(i)} - p_{\text{ref}}^{(i)}\right)^2}}{\sqrt{\sum_i \left(p_{\text{ref}}^{(i)}\right)^2}} \tag{32}$$

with the stresses evaluated in the third medium, on its interface to the lower block, at 11 points starting from the vertical plane of symmetry, see markers (+) in Fig. 4, hence capturing the zone of highest contact pressures.

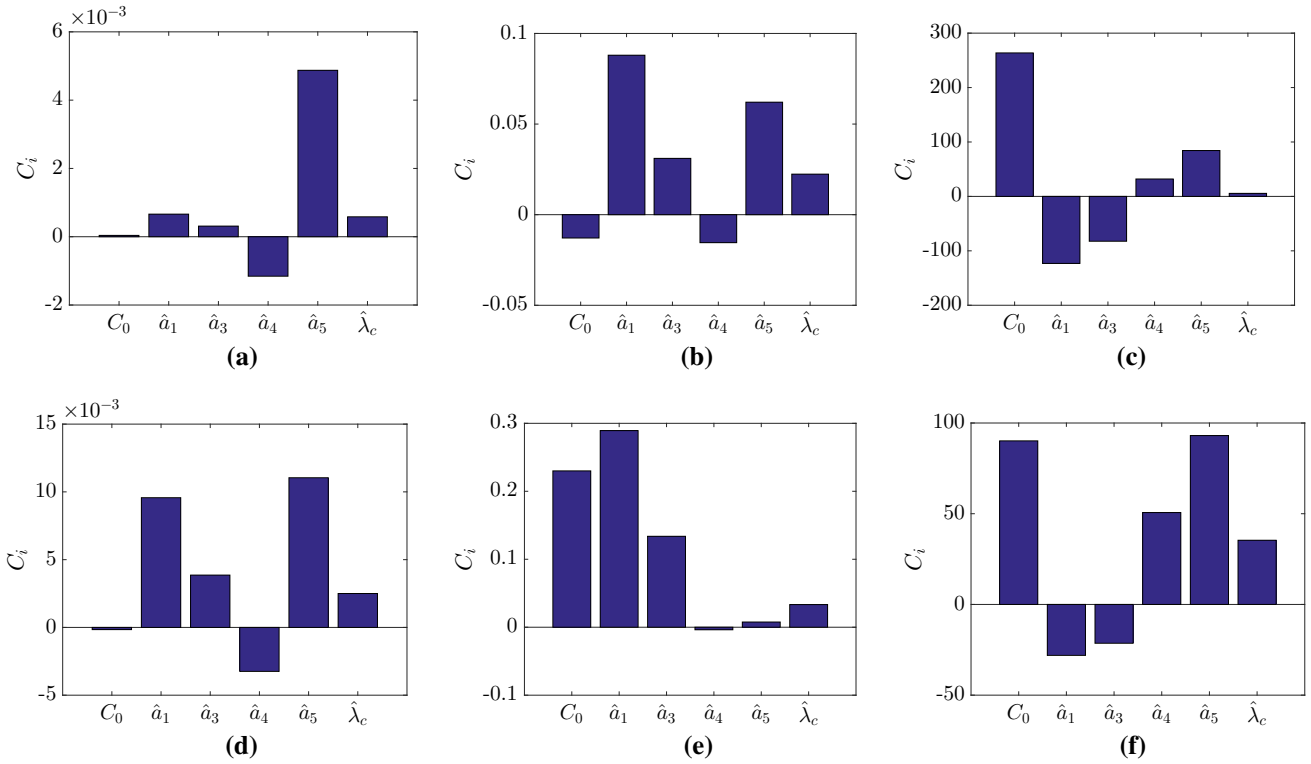

Fig. 5 Hertz example: influence of the (normalized) parameters $\hat{a}_1, \ldots, \hat{\lambda}_{\text{thr}}$ on gap size (**a**, **d**), pressure error p_{err} (**b**, **e**), and number of iterations N_{iter} (**c**, **f**). Top row: geometry 1, base material 1, highest load. Bottom row: geometry 2, base material 2, lowest load

- Number of iterations: the total number N_{iter} of Newton–Raphson iterations, over all load steps, needed for convergence.

An exemplary contact pressure distribution obtained with the third medium approach is shown in Fig. 4. It is evident that the analytical pressure distribution, which features a C^0 point at the boundary between contact and no-contact regions, is approximated by the third medium method through a smooth curve. Nevertheless, a good agreement between the two distributions is achieved in the central region of highest contact pressure. Note also that the values of σ_{yy} for the third medium, evaluated at the interface with the lower block, are intermediate between those for the upper cylinder and the lower block at the respective interfaces with the third medium.

To translate the results into an optimal choice of the material parameters for the third medium, the following two strategies were used:

1. For each load case, material combination for the contacting bodies and geometry, the distribution of the gap sizes and pressure errors was calculated, and the parameter combination from Table 2 which yields errors in the lowest percentile with the lowest number of iterations was selected.
2. To quantify and compare the strength of the relationship between the quantities of interest (gap size, pressure error, and number of iterations) and the individual parameters in the material model for the third medium, multidimensional linear regression was used, fitting the model

$$C_0 + C_1\hat{a}_1 + C_2\hat{a}_3 + C_3\hat{a}_4 + C_4\hat{a}_5 + C_5\hat{\lambda}_c \tag{33}$$

to gap size, pressure error, and number of iterations. The parameters marked by hât denote the parameters $\tilde{a}_1$ to λ_c linearly rescaled to the interval [0, 1], so that the fitted coefficients C_i directly reflect the effect of the respective parameters *within their given range*.

The results from the multidimensional linear regression are presented first. For brevity, Fig. 5 depicts the results for geometry 1, material combination 1, the highest load, and geometry 2, material combination 2, the lowest load, considering that the other results varied within the range of these two extreme combinations, see Annex 1. What is desired from the "quality measures" gap size, pressure error and number of iterations is that they are all as low as possible. For this purpose, the constant term C_0 should be low compared to the other coefficients, and the parameters should ideally have positive *or*

Table 3 Hertz example: material parameters of the third medium which yield the best agreement between third medium and analytical results, with lowest number of iterations required

Percentile	$\tilde{a}_1, \tilde{a}_2$	$\tilde{a}_3$	a_4	$\tilde{a}_5$	λ_c
10%	3×10^{-4}	10^{-4}	1	2×10^{-7}	0.3–0.5
20%	3×10^{-4}	3×10^{-4}	1–23	2×10^{-7}	0.1–0.5
30%	3×10^{-4}	10^{-3}	1–23	2×10^{-7}	0.1–0.5

negative regression with all measures. The following observations stem from the results in Fig. 5:

- Gap size and pressure error change in the same direction. This is reasonable as a smaller gap size implies a contact geometry closer to the one predicted by the Hertz theory, leading in turn to a more accurate pressure distribution.
- The isotropic stiffness ($a_1 = a_2, a_3$) has a high influence on the pressure error, whereas the gap size is more influenced by the anisotropic stiffness (a_5).
- Apart from a_5 and λ_c, for which the lowest value is the best choice for all quality measures, for all other parameters a decrease of gap size and pressure error has a negative effect on the number of iterations.
- The pressure error can be reduced less for a lower load than for a higher load.

These results are expected: the third medium, being fictitious, should have a stiffness as low as possible in the pre-contact regime, but this choice is limited by the issue of numerical stability, especially in the force control conditions adopted here. The findings furthermore match the results by Bog et al. [4], where likewise a low stiffness led to a smaller remaining gap, but decreased stability.

From the individual simulation results follow the optimal parameter combinations in Table 3. They confirm the conclusions that a_5 should be chosen as low as possible, λ_c plays only a minor role, while for the other parameters a compromise between accuracy and efficiency must be sought.

4.2 Sliding contact

With this example, the systematic assessment in Sect. 4.1 is performed again for a frictionless contact simulation with significant sliding. The geometry is shown in Fig. 6. The boundary conditions are: bottom edge fixed, top edge moved down by 0.12 units, then moved sidewards. An exemplary deformed shape is depicted in Fig. 7. The procedure for identification of the optimal material parameters of the third medium for this example follows the same lines as for normal contact in the previous example. As target quality parameter, the following measure was chosen:

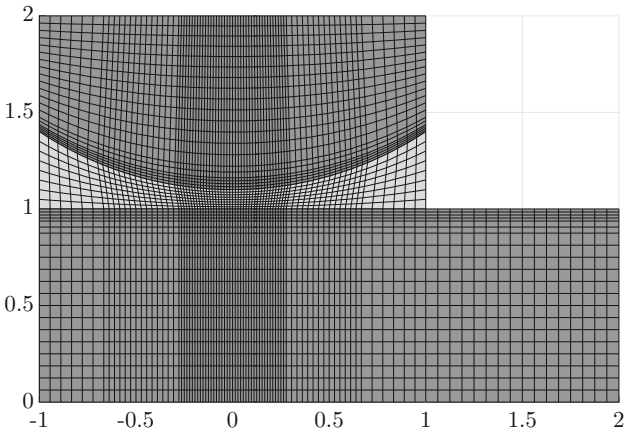

Fig. 6 Sliding problem. Upper cylinder is pressed to lower block and then moved horizontally

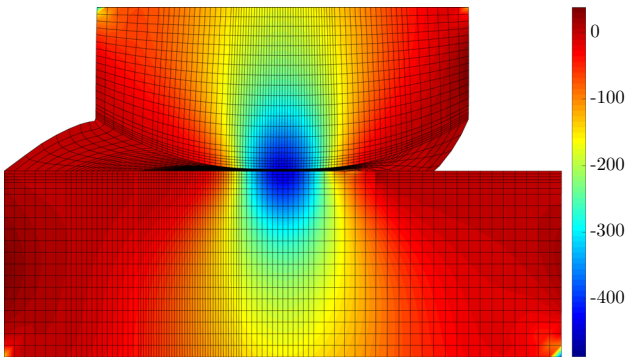

Fig. 7 Sliding example: deformed shape at downward displacement of 0.12 units and sideward displacement of 0.5 units. Color coding visualizes stress σ_{yy}. Material properties: $(E_1, \nu_1) = (7000, 0.3)$, $(E_2, \nu_2) = (70000, 0.45)$, $(\tilde{a}_1, \tilde{a}_2, \tilde{a}_3, a_4, \tilde{a}_5, \lambda_c) = (3 \cdot 10^{-4}, 3 \cdot 10^{-4}, 10^{-4}, 1, 10^{-5}, 0.5)$

- Apparent friction coefficient μ^*: ratio of total horizontal to total vertical reaction force. Since this ratio is not constant during sliding, it was conventionally evaluated at a lateral displacement of 0.1 units.

A typical course of the vertical and horizontal reaction force is shown in Fig. 8. One notices an unwanted increase in horizontal force with increasing amount of sliding, which is not reverted during vertical unloading (with horizontal displacement still present). This is mostly the result of the isotropic stiffness of the medium, which even after unloading experiences significant amounts of shear.

On the effect of individual parameters, see Fig. 9, one again observes the strong influence of a_5, which should be chosen as low as possible for minimum apparent friction. That the anisotropic stiffness represented by a_5 influences the tangential force may appear surprising at first, but it has to be considered that the equivalence of surface normal $\mathbf{N}$ and direction of maximum compression $\mathbf{e}$ is only valid in

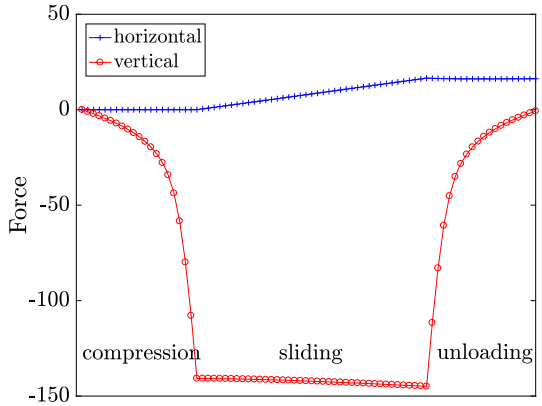

Fig. 8 Sliding example: change of reaction force upon compression, sliding, and vertical unloading

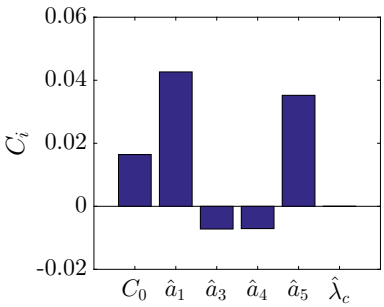

Fig. 9 Sliding example: influence of the (normalized) parameters $\hat{a}_1, \ldots, \hat{\lambda}_{\text{thr}}$ on the apparent friction coefficient

the limit of diminishing gap size. With high values of a_5 leading to a large gap, the likelihood of mismatch between the two directions increases. As expected, low isotropic stiffness a_1, a_2 decreases the shear stiffness of the third medium, hence lowers the apparent friction. All other parameters have only minor influence.

It is furthermore noteworthy that the constant term of the apparent friction coefficient is below 2%, which may be rated frictionless for most practical applications. Analogously to Tables 3 and 4 reports the optimal parameters directly chosen from the individual simulation results, along with the amount of sliding before iterative convergence could no longer be reached. The latter quantity was found to depend strongly on the settings of the numerical procedure, including displacement increment, tolerance and maximum number of iterations of the Newton–Raphson scheme, here respectively set to $\Delta u = 0.01$, $|\mathbf{R}|_{\text{tol}} = 10^{-6}$ and $N_{\max} = 8$.

In comparing both tables, it turns out that there is no perfect match between the optimal parameter combinations in normal and sliding contact, but the 20% percentiles mostly agree, such that the parameters summarized in Table 5 offer the best compromise.

Table 4 Sliding example: material parameters of the third medium which result in the lowest apparent friction coefficient, and corresponding maximum amount of sliding $u_{\max}$

Percentile	$\tilde{a}_1, \tilde{a}_2$	$\tilde{a}_3$	a_4	$\tilde{a}_5$	λ_c	$u_{\max}$
10%	10^{-4}	10^{-3}	1–23	2×10^{-7}	0.1–0.5	0.3
20%	10^{-4}	3×10^{-4}	1–23	2×10^{-7}	0.1–0.3	0.45
30%	10^{-4}	3×10^{-4}	1	2×10^{-7}	0.3	0.45

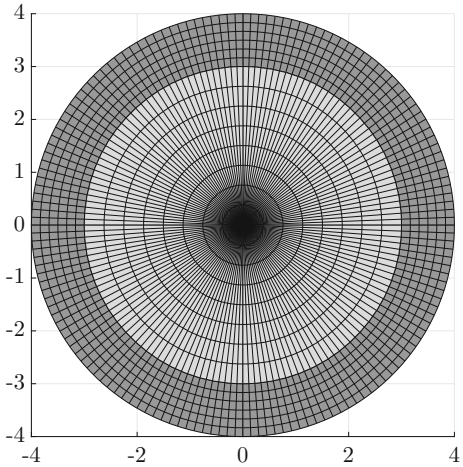

Fig. 10 Self contact example, undeformed geometry: hyperelastic ring with embedded third medium

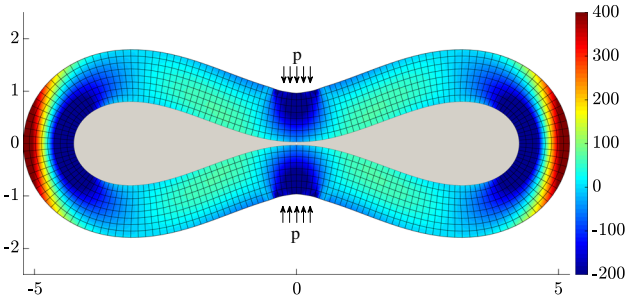

Fig. 11 Self contact example: pinched hyperelastic ring with embedded third medium (gray). Color shows stress σ_{yy} at a load of $P_{\text{total}} = 56.1$ units, which, without third medium, would just lead to self contact. The residual gap size is approximately 2% of the initial separation. (Color figure online)

4.3 Self contact and confined compression

An application were the third medium method can be especially useful is self contact in complex geometries, most notably in porous media. By simply filling any cavity with the third medium, the possibility of self contact can be dealt with automatically without the need for contact formulations. However, in such situations the third medium is often in a state of confined compression, and it is unclear if the parameters found in the previous section are adequate. Consequently, an additional example as shown in Figs. 10 (undeformed) and 11 (deformed) is considered: a hyperelastic ring with

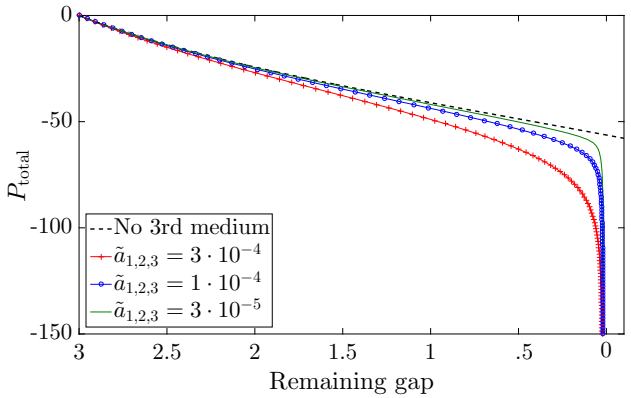

Fig. 12 Self contact example: effect of the presence of third medium on the force-separation relation in the pinched cylinder for three different isotropic stiffnesses

Table 5 Parameter combination for the third medium which yields optimal performance in both, the Hertzian contact and the finite sliding examples

$\tilde{a}_1, \tilde{a}_2$	$\tilde{a}_3$	a_4	$\tilde{a}_5$	λ_c
$1\text{–}3 \times 10^{-4}$	3×10^{-4}	1	2×10^{-7}	0.3

$\mu = \Lambda = 1000$ is filled with the third medium and pinched by applying a uniform vertical traction p over the six central elements. Bearing the symmetry of the problem in mind, only one-quarter of the ring was modeled, and all quantities (total force P_{total}, gap) are related to this quarter ring. As usual, by applying a total load that, without third medium, would just lead to self contact, a gap between the two halves of the ring remains, though it is small compared to the initial separation at this point. It is desired that the presence of the third medium does not cause any additional stiffness in the system before contact occurs. In Fig. 12, the total force for pinching the ring is plotted as a function of the remaining gap, for the ring with a third medium of different isotropic stiffnesses. With the optimal parameter combination identified in Table 5 (with $\tilde{a}_1 = 3 \cdot 10^{-4}$), a rather high additional stiffness is introduced into the system. Decreasing the stiffness parameters $\tilde{a}_{1,2,3}$ by a factor of 10, the force-displacement relation becomes very close to that of the unfilled ring in the pre-contact regime. Such a low stiffness is both feasible and necessary here as the third medium cannot deform freely as in the contact examples in Sects. 4.1 and 4.2.

The simulation of the pinched hyperelastic ring (Fig. 11) is repeated in three dimensions, see Fig. 13. Also in this case, the third medium successfully prevents self contact, while allowing for a gap between the ring segments of less than 1% of the initial separation.

4.4 Spatial convergence

The third medium method replaces the original non-smooth contact problem by a smooth continuum mechanical problem. As a result, it is expected to achieve the spatial convergences rates associated with smooth problems. These increase with the order of the discretization, which can be arbitrarily raised within IGA with no changes in the discretized geometry. To verify this, for the contact problem in Fig. 3a, the rate of spatial convergence in the L^2 norm of stress σ_{yy}

$$e_{L^2}^{\sigma_{yy}} = \frac{\sqrt{\sum_i \left(\sigma_{yy}^{(i)} - \sigma_{yy,\text{ref}}^{(i)}\right)^2}}{\sqrt{\sum_i \left(\sigma_{yy,\text{ref}}^{(i)}\right)^2}} \tag{34}$$

was calculated for different approximation orders p. Herein, the stress is evaluated at 100 equally-spaced positions in the region spanning 0.3 units from the center line, in the third medium at its interface with the lower block. As reference solution, an overkill simulation of same order p with a mesh density two times higher, in each parametric direction, than the finest mesh in the convergence plot was used. Note that the stress distribution will not converge to the analytical (Hertzian) one, hence this cannot be used as reference. The result is depicted in Fig. 14. A clear increase in the rate of convergence with the discretization order is observed. The

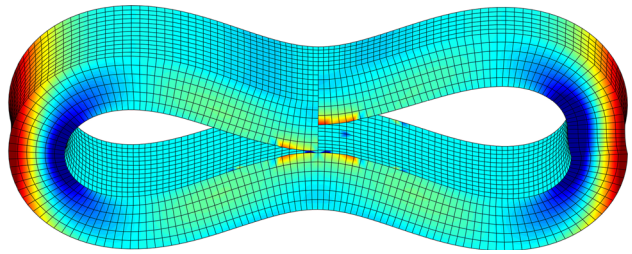

Fig. 13 Self contact example in three dimensions: pinched hyperelastic ring with embedded third medium (not shown). Color shows stress σ_{yy} at a residual gap of approximately 0.7% of the initial separation. Upper right segment removed to show interior

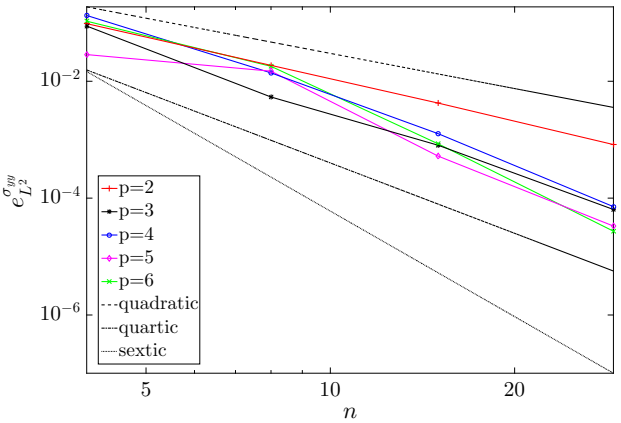

Fig. 14 Spatial convergence: error in contact pressure versus number of elements n in the contact zone, for different approximation orders p

Table 6 Comparison between IGA and FEM for different discretization orders p: maximum vertical displacement $v_{\max}$ before iterative convergence could no longer be achieved

	$p=1$	$p=2$	$p=3$	$p=4$
(a)				
IGA	–	0.245	0.210	0.200
FEM-EL	0.055	0.055	0.055	0.055
FEM-DOF	0.055	0.055	0.055	0.055
(b)				
IGA	–	0.205	0.180	0.180
FEM-EL	0.110	0.110	0.110	0.110
FEM-DOF	0.110	0.110	0.110	0.110

Geometry (a) from Fig. 3, initial gap of 0.05 units (a), geometry (b), initial gap of 0.1 units (b)

rate is roughly equal to p as expected for a smooth continuum mechanical problem.

4.5 Comparison of FEM and IGA

IGA was demonstrated to be robust against mesh distortion in some situations [7], which motivates us to investigate if there is an advantage of IGA over higher-order FEM in contact using the third-medium method. To this end, the two Hertzian contact examples were rerun with conventional FEM, using the parameters in Table 5. Starting with the same NURBS geometry, each IGA element was replaced by a serendipity element of equal order (FEM-EL). Note that, for a fixed number of elements, the number of degrees of freedom in FEM will be significantly higher than in IGA (factor of 2.8 at $p = 2$ and 6.0 at $p = 4$). Consequently, an additional finite element discretization with less elements was also considered, in which the number of degrees of freedom is approximately equal to that of the IGA case (FEM-DOF). For the sake of completeness, linear elements were also included in the comparison. To quantify the robustness of the methods, we recorded at what vertical displacement $v_{\max}$ iterative convergence could no longer be attained, with displacement increments of $\Delta v = 0.005$. The results are presented in Table 6. Conventional FE fails at a displacement slightly higher than the initial gap between the bodies, whereas IGA allows for substantially higher compression. Inspection of the stress distribution at the last converged displacement increment reveals that the difference between IGA and FEM results is small. However with FEM stress oscillations develop near the corners of the interface between the third medium and the lower block, whereas using IGA only stress concentrations occur. Interestingly, the robustness of FEM is unaffected by the degree of the discretization, whereas for IGA it seems that the robustness decreases as the order increases. Nevertheless, even the worst results are still significantly better than FEM results.

A detailed comparison of the computational cost is out of our scope. However, it is already known that, for the same number of elements, the computational effort in FEM and IGA is comparable, whereas for the same number of degrees of freedom FEM is faster especially for higher orders; a detailed study can be found in [10].

5 Conclusions

In this work, the third medium method for contact between deformable bodies, originally proposed in [3], was combined with isogeometric analysis (IGA). The method transforms the original non-smooth contact problem into a smooth continuum mechanical problem.

One of the objectives of the present paper was the proper choice of the parameters in the third medium constitutive model. The presented examples demonstrated that it is imperative to choose the isotropic as well as anisotropic stiffnesses of the third medium such that they are considerably smaller than the stiffnesses of the bodies in contact. This guarantees that the remaining artificial gap between the bodies is minimized, no significant additional stiffness is inserted in the system, and frictionless contact (tangential traction very small compared to normal traction) is accurately approximated. However, the choice of the parameters is also influenced by the requirement of stability, which in turn depends on whether force or displacement control is utilized, and on whether the medium can deform freely or not. An excessively low stiffness can result in the inability to achieve iterative convergence even for very small load increments, and thus in the need for more advanced numerical solution methods, see also [4].

An additional focus on the paper was to explore the use of the third medium method in combination with higher-order discretizations in IGA. The smooth nature of the problem solved with the method in combination with the use of higher-order discretizations was demonstrated to lead to the possibility to achieve higher-order spatial convergence rates. Comparison with conventional higher-order finite elements in Hertzian contact revealed a higher stability of IGA, allowing for larger deformations and contact pressures. Overall, it was shown that substantial amounts of deformation in the third medium are possible, such that the isogeometric third medium method appears suitable for a large number of applications. Finally, we investigated self contact as an attractive application of the third medium approach.

In the present work such as in [3], elastic behavior was assumed for the third medium, which was consistent with the study of frictionless contact. In order for frictional contact to be tackled with a third medium approach, a source of

dissipation must be incorporated in the material modeling of the third medium; e.g., through an elasto-plastic constitutive behavior. This and additional aspects are open questions for further research.

Acknowledgements The authors at the TU Braunschweig wish to acknowledge funding from the European Research Council, ERC Starting Researcher Grant INTERFACES, Grant Agreement N. 279439.

Annex

Hertzian contact: effect of material parameters

See Figs. 15 and 16.

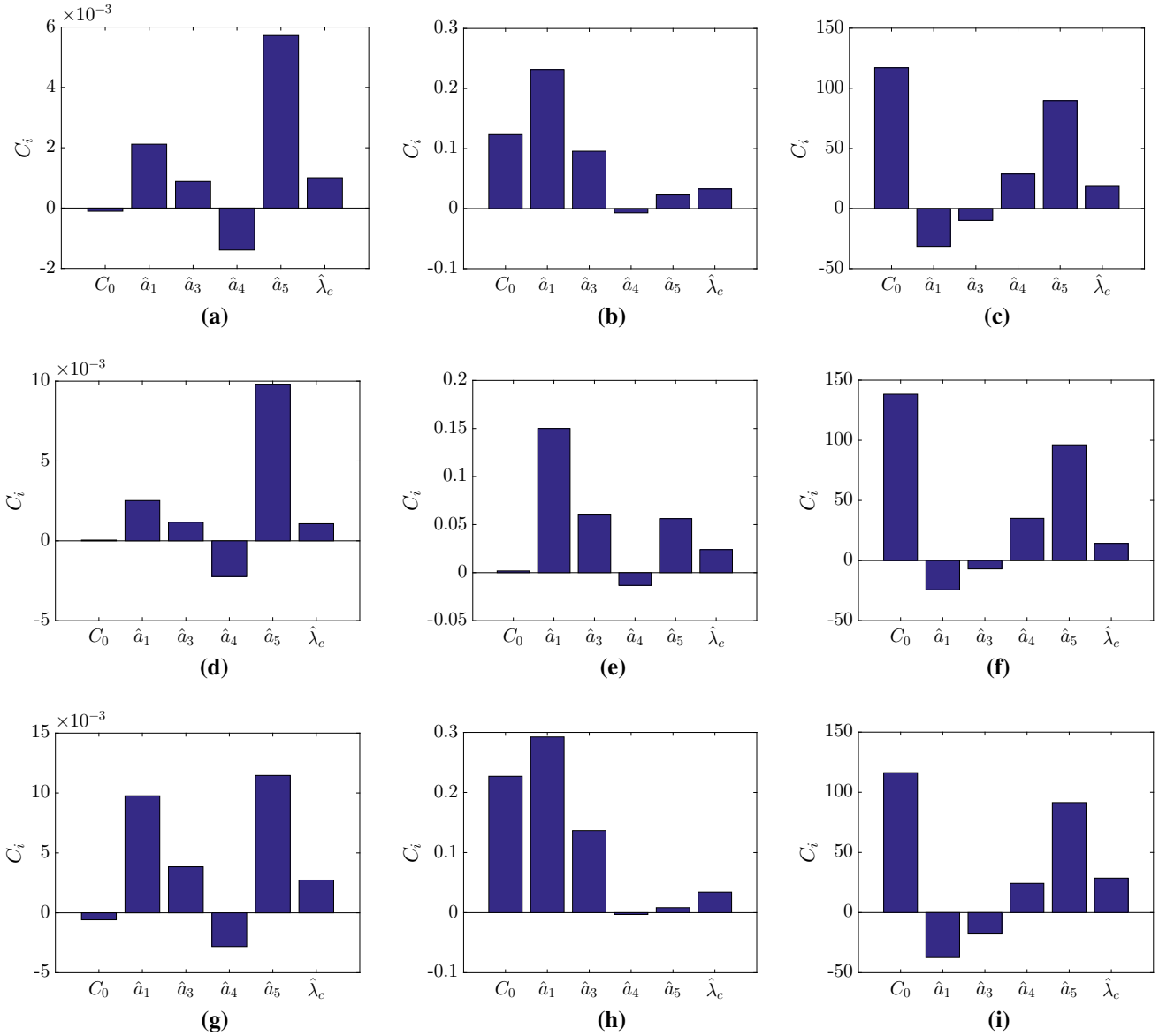

Fig. 15 Hertz example, geometry 1: influence of the (normalized) parameters $\hat{a}_1, \ldots, \hat{\lambda}_{\text{thr}}$ on gap size (**a**, **d**, **g**), pressure error p_{err} (**b**, **e**, **h**), and number of iterations N_{iter} (**c**, **f**, **i**). Top row: base material 1, lowest load. Center row: base material 2, highest load. Bottom row: base material 2, lowest load

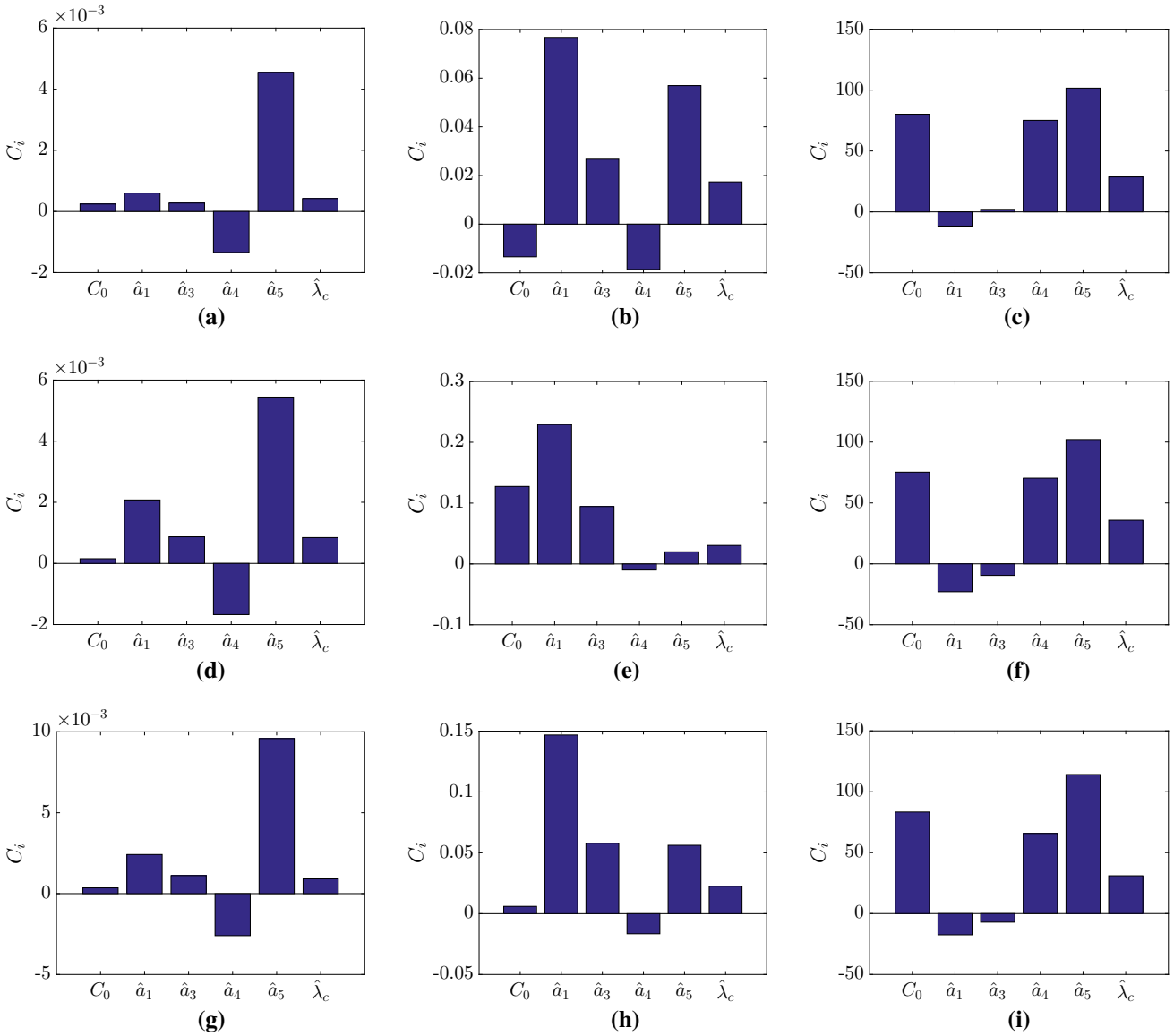

Fig. 16 Hertz example, geometry 2: influence of the (normalized) parameters $\hat{a}_1, \ldots, \hat{\lambda}_{\text{thr}}$ on gap size (**a**, **d**, **g**), pressure error p_{err} (**b**, **e**, **h**), and number of iterations N_{iter} (**c**, **f**, **i**). Top row: base material 1, highest load. Center row: base material 1, lowest load. Bottom row: base material 2, highest load

References

1. Wriggers P (2002) Computational contact mechanics. Wiley, West Sussex
2. Laursen TA (2002) Computational contact and impact mechanics. Springer, Berlin
3. Wriggers P, Schröder J, Schwarz A (2013) A finite element method for contact using a third medium. Comput Mech 52:837–847
4. Bog T, Zander N, Kollmannsberger S, Rank E (2015) Normal contact with high order finite elements and a fictitious contact material. Comput Math Appl 70:1370–1390
5. Hughes TJR, Cottrell JA, Bazilevs Y (2005) Isogeometric analysis: CAD, finite elements, NURBS, exact geometry and mesh refinement. Comput Methods Appl Mech Eng 194:4135–4195
6. De Lorenzis L, Hughes TJR, Wriggers P (2014) Isogeometric contact: a review. In: GAMM Mitteilungen, pp. 85–123
7. Lipton S, Evans JA, Bazilevs Y, Elguedj T, Hughes TJR (2010) Robustness of isogeometric structural discretizations und severe mesh distortion. Comput Methods Appl Mech Eng 199:357–373
8. Cottrell J Austin, Hughes Thomas JR, Bazilevs Y (2009) Isogeometric analysis: toward integration of CAD and FEA. Wiley, New York
9. Johnson KL (2003) Contact mechanics. Cambridge University Press, Cambridge
10. Schillinger D, Evans JA, Reali A, Scott MA, Hughes TJR (2013) Isogeometric collocation: cost comparison with Galerkin methods and extension to adaptive hierarchical NURBS discretizations. Comput Methods Appl Mech Eng 267:170–232